NANO LETTERS
Letter
pubs.acs.org/NanoLett

Tuning the Built-in Electric Field in Ferroelectric $Pb(Zr_{0.2}Ti_{0.8})O_3$ Films for Long-Term Stability of Single-Digit Nanometer Inverted Domains

Noureddine Tayebi,[*,†,‡] Sunkook Kim,[†,§] Robert J. Chen,[†] Quan Tran,[†] Nathan Franklin,[†] Yoshio Nishi,[‡] Qing Ma,[†] and Valluri Rao[†]

[†]Intel Corporation, 2200 Mission College Boulevard, Santa Clara, California 95054, United States
[‡]Department of Electrical Engineering, Stanford University, 420 Via Palou Mall, Stanford, California 94305, United States
[§]Department of Electronics and Radio Engineering, Institute for Laser Engineering, Kyung Hee University, Gyeonggi, 446-701, South Korea

Supporting Information

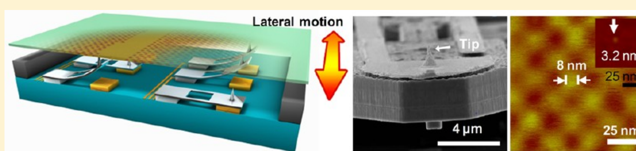

ABSTRACT: The emergence of new technologies, such as whole genome sequencing systems, which generate a large amount of data, is requiring ultrahigh storage capacities. Due to their compactness and low power consumption, probe-based memory devices using $Pb(Zr_{0.2}Ti_{0.8})O_3$ (PZT) ferroelectric films are the ideal candidate for such applications where portability is desired. To achieve ultrahigh (>1 Tbit/in^2) storage densities, sub-10 nm inverted domains are required. However, such domains remain unstable and can invert back to their original polarization due to the effects of an antiparallel built-in electric field in the PZT film, domain-wall, and depolarization energies. Here, we show that the built-in electric-field can be tuned and suppressed by repetitive hydrogen and oxygen plasma treatments. Such treatments trigger reversible Pb reduction/oxidation activity, which alters the electrochemistry of the Pb overlayer and compensates for charges induced by the Pb vacancies. This tuning mechanism is used to demonstrate the writing of stable and equal size sub-4 nm domains in both up- and down-polarized PZT films, corresponding to eight inverted unit-cells. The bit sizes recorded here are the smallest ever achieved, which correspond to potential 60 Tbit/in^2 data storage densities.

KEYWORDS: *Ultrahigh density memory, ferroelectric films, single-digit nanometer inverted domains, probe-based storage*

Due to their fast, electrically switchable polarization, single crystalline $Pb(Zr_{0.2}Ti_{0.8})O_3$ (PZT) ferroelectric oxide have been extensively used as write-and-read media in ferroelectric-random-access memory (FeRAM)[1,2] and ultra-high-density (>1 Tbit/in^2) probe-based memory devices.[3−11] In the latter case, a short electrical pulse is applied on the ferroelectric medium through a conductive atomic-force-microscope-like cantilever probe.[3−11] The highly concentrated electric field between the probe and the bottom electrode can invert the polarization of a local medium volume, resulting in a nonvolatile ferroelectric domain that is the basis of data recording. Our group has recently developed an ultrahigh density probe memory device based on microelectromechanical system (MEMS) technology (Figure 2a),[11] whereby 5000 cantilever probes (Figure 1b,c), with sub-50 nm tips and spaced at a 150 μm pitch, can be used in parallel to write and read data on an integrated nonvolatile PZT medium.[11] The probe array is integrated with standard complementary metal−oxide−semiconductor (CMOS) substrates and is controlled by a MEMS mover with sub-nanometer precision over >150 μm strokes. As shown in Figure 1d, this writing mechanism can generate densities as large as 3.6 Tbit/in^2 with 8-nm inverted domain sizes.

For this technology to be viable, single-digit nanometer inverted domains, which are required for ultrahigh-density (>1 Tbit/in^2), have to remain stable over the device lifetime. Our group has recently demonstrated that such domains can remain stable only if they are fully inverted through the entire ferroelectric film thickness, which is dependent on a critical ratio of electrode size to film thickness.[12] Under full inversion condition, the forces exerted by the depolarization (electrostatic) and domain-wall energies are reduced. Since such small domains can only be obtained using ultra sharp probe-tips, thinner ferroelectric films are required to enable their stability.[12] Such thin films are also required to meet the demands for high speed-switching and data reads. However, there is a critical film thickness limit below which the ferroelectric film properties vanish due solely to the depolarization (electrostatic) field.[13] This thickness has been estimated to be around 1.2−5 nm for both PZT[14−16] and $BaTiO_3$[14,17,18] films. Therefore, there is a limit to the PZT film thickness, although it was shown recently that highly strained $BaTiO_3$ films may retain their ferroelectric properties down to 1 nm thickness, that is, below the critical thickness limit.[8] Moreover and due to their high partial pressure, Pb atoms can readily evaporate during PZT film growth,[19] creating vacancies

Received: May 1, 2012
Revised: October 6, 2012
Published: October 8, 2012

ACS Publications © 2012 American Chemical Society

dx.doi.org/10.1021/nl302911k | *Nano Lett.* 2012, 12, 5455−5463

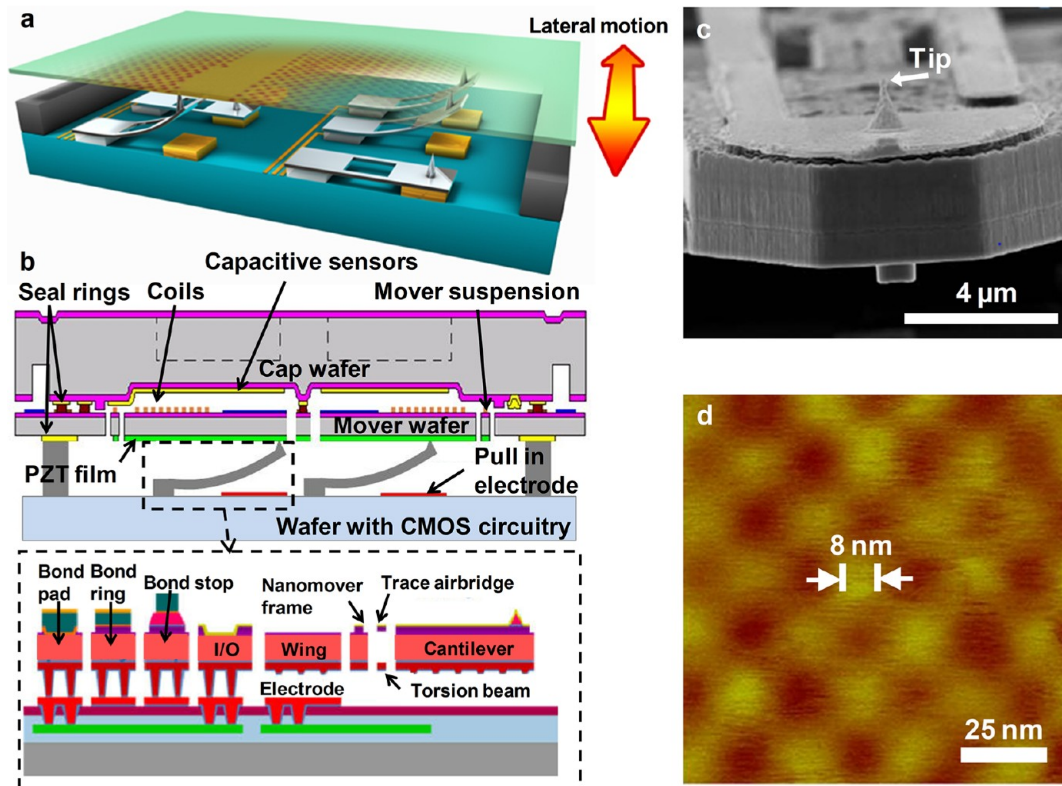

Figure 1. Ultrahigh density MEMS probe memory device fabricated on a CMOS substrate and integrated with a PZT ferroelectric medium. (a) Schematic of the MEMS probe memory device in writing mode. (b) Schematic of probe memory device architecture. The inset shows cantilever probe architecture interfaced with vias and CMOS readout circuitry (see ref 11 for more details). (c) Scanning electron microscope (SEM) image of a cantilever probe. (d) A 3.6 Tbit/in^2 checkerboard writing on the PZT film with 8-nm inverted domains.

that act like acceptor impurities, that is, as grown PZT films act as *p*-type semiconductors. This, in turn, induces an antiparallel built-in electric field (E_b) due to trapped negative charges originating from these vacancies that are mainly at the exposed surface. Thinner PZT films can, therefore, cause an increase in the density of Pb vacancies and thus increasing E_b. This increase exacerbates the effects of sub-10 nm inverted domain instability in probe-based storage[12,20,21] and media fatigue in FeRAMs.[22]

Here, we show that the built-in electric-field is mainly due to near-surface trapped negative charges and can be tuned and suppressed by repetitive hydrogen and oxygen plasma treatments. Such treatments trigger reversible Pb reduction/oxidation activity, thereby altering the electrochemistry of the Pb overlayer, which compensates for charges induced by the Pb vacancies. Here, the term "Pb overlayer" commonly refers to Pb in the surface layer of the PZT film. The charge compensation and the vacancy doping mechanisms at the PZT surface are confirmed with electrical and X-ray photoelectron spectroscopy characterizations of the PZT films. Furthermore, this tuning mechanism is used to demonstrate the writing of stable and equal size sub-4 nm domains in both up and down-polarized PZT films, corresponding to eight inverted unit-cells. The bit sizes recorded here are the smallest ever achieved, which correspond to potential 60 Tbit/in^2 data storage densities.

In principle, compensating for these trapped negative charges will reduce E_b. Impurity doping mechanisms have already been proposed for vacancy charge compensation in ABO_3 ferroelectric materials.[23] These include Fe, Mn, Cu, and Gd.[23] However, such dopant ions can be incorporated simultaneously on A- and B-sites,[23] which does not provide a robust way to precisely tune and suppress E_b. Moreover, this mechanism affects the conductivity and dielectric constant of the ferroelectric materials.[23]

The formation of defects including lead vacancies (V_{Pb}^{-2}) and O vacancies (V_O^{+2}) under oxygen-rich (oxidizing) and oxygen-poor (reducing) environments has recently been investigated theoretically using ab initio studies for $PbTiO_3$[24−26] and $PbZrO_3$.[26] Note that $PbTiO_3$ and $PbZrO_3$ are the two systems that compose the PZT material. Under the oxygen-poor (reducing) conditions, both O and Pb vacancies possess negative formation energies. Therefore, both vacancies are susceptible to form under these conditions. The creation of large density of O vacancies under oxygen-poor conditions will affect the initial *p*-type conductivity of the PZT film. It will also reduce, suppress, or even change the direction of the built-in electric field if the O vacancies exceed the Pb ones. On the other hand, O vacancies possess highly positive formation energy and are not stable under oxygen-rich (oxidizing) conditions.[24] Therefore, the Pb vacancies cannot be compensated for. In fact, any O and Pb vacancies that might have been present will be filled by O atoms, thereby oxidizing Pb. Such a mechanism will exacerbate the effect of the built-in electric field and will increase the acceptor doping density. Ti and Zr vacancies also possess very highly positive formation energies and are not susceptible to form in either conditions.[24−26]

To create oxygen-poor and oxygen-rich conditions, we use hydrogen (H_2) and oxygen (O_2) plasma treatments, respectively. During the H_2 plasma treatment, near PZT surface oxygen reacts with hydrogen to create O vacancies and

reduce Pb, whereas during the O_2 plasma treatment, vacancies are filled with O atoms. Our study is performed on atomically smooth, single crystalline PZT films deposited on single crystalline $SrRuO_3$−$SrTiO_3$(100) substrate systems using metal−organic chemical vapor deposition (MOCVD). The 50 nm thick perovskite $SrRuO_3$ (SRO) intermediate film is used to facilitate the heteroepitaxy and is epitaxially deposited on $SrTiO_3$(100) (STO) single crystal substrate at ∼650 °C with a DC sputtering approach (with O_2/Ar at 10 mTorr) in which SrRu was used as sputtering target. It also serves as a conducting bottom electrode for piezoresponse force microscopy and electrical characterization of the PZT films.

The PZT film is then deposited at a 605 °C temperature under a 5 Torr pressure with Ti and Zr precursor fluxes maintained at 0.07 mL/min and 0.025 mL/min. To obtain atomically smooth PZT surfaces, the Pb flux has to be maintained at an optimum value of 0.165 mL/min, whereby a two-dimensional, that is, layer-by-layer, growth mode is obtained with root-mean-square (RMS) roughness of 0.17−0.21 nm. Increasing or decreasing the Pb flux away from this optimum value results in a rough (RMS roughness 0.6 nm), three-dimensional growth (see Supporting Information for further details). Figure 2a shows an atomic force microscopy

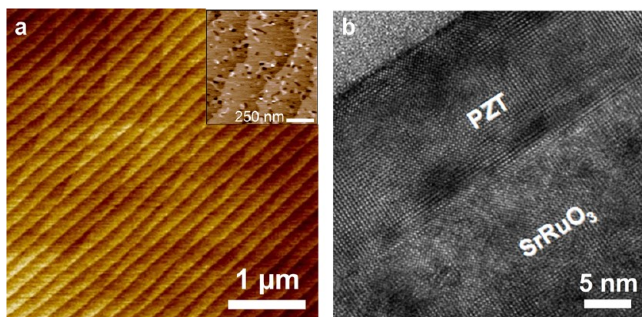

Figure 2. Atomically smooth, two-dimensional PZT ferroelectric film grown at the optimized Pb flow rate using the MOCVD technique. (a) Large ($4 \times 4\ \mu m^2$) AFM topographic height image of a 17 nm thick PZT film. Inset shows a higher resolution $1 \times 1\ \mu m^2$ topographic height image. (b) Cross-sectional transmission electron microscopy (XTEM) image of the same film.

(AFM) scan of the PZT surface where ordered arrays of terraces separated by one-unit-cell atomic steps area revealed. Figure 2b shows a transmission electron microscopy (TEM) image of the 17 nm thick PZT film grown at the optimized conditions in which the single crystallinity of the film is seen. Moreover, X-ray θ−2θ scans of the PZT/SRO/STO system reveal only diffraction peaks from the substrate and (001) reflections from the heterostructure. No reflections that would be indicative of second phases were observed (see Supporting Information).

Electrical characterization of the 17 nm thick PZT film is performed by depositing 25 nm thick Pt pads ($25 \times 25\ \mu m^2$ in size) on the PZT films to serve as top electrodes (see Supporting Information). Pt is used to avoid oxygen vacancy formation at the PZT surface due to exposure to oxidizing metal pads such as Ti, which in turn can affect the electrical characteristics of the film, thereby compensating for the Pb vacancies and providing wrong estimates of the actual built-in electric field and equivalent doping densities of the PZT film. Moreover, Pt and SRO possess almost the same work function ($\phi_{M(Pt)}$ = 5.3 eV and $\phi_{M(SRO)}$ = 5.2 eV), which reduces the system asymmetry. Note that previous studies have shown that Pt electrodes could react with Pb near the PZT surface to create a stable Pb_xPt_{1-x} phase.[27] This reaction appeared to cause the formation of nonferroelectric layer at the PZT/electrode interface. However, such a reaction was only seen in polycrystalline PZT films where a Pb rich carbonate-like surface layer is known to form.[28] This is very likely due to the segregation or trapping of Pb atoms in grain boundaries close to the surface during deposition. This, however, has not been reported for single-crystalline PZT films.

Figure 3a,b shows the capacitance−voltage (C−V) and polarization−voltage (P−V) hysteresis loops. Very good butterfly-like capacitance variation and square-like hysteresis loop with high switching speeds are observed. $+V_s$ and $-V_s$ are the positive and negative switching biases that describe the transition of reverse junction capacitance from the bottom-to-top and top-to-bottom Schottky contacts. $+P_r$ and $-P_r$ are the positive and negative remnant polarizations at the bottom and top contacts. It is clearly seen from the C−V hysteresis loop that $+V_s$ and $-V_s$ switching biases are different, which is a departure from the ideal back-to-back Schottky diode model. This phenomenon strongly supports the presence of a remnant polarization originating from negative trap charges giving rise to a parallel shift of the C−V curves associated with bias direction. The remnant polarization is independent of the bias except within the reverse polarization regime as shown in the polarization hysteresis loop (Figure 3b). The cross point (positive voltage shift) of the butterfly C−V curve, X_{pt}, is a measure of E_b induced by the Pb vacancies. The flat-band voltage shift due to these trap charges can be fully described by Gauss's law (see subsequent sections). Note also that the switching speed of down (∼201.4 μC/V cm^2) and up (∼250.2 μC/V cm^2) polarization are different as shown in the P−E curve (Figure 3b). This is consistent with the fact that the remnant polarizations $-P_r$ and $+P_r$ lead to different positive and negative switching biases as observed in the C−V curve (Figure 3a).

To understand the charge compensation and the vacancy doping mechanisms at the PZT surface that enable E_b tuning proposed in the subsequent section, we have developed a C−V model for the metal−ferroelectric−metal (MFM) system. The validation of this model is facilitated by the ideal properties of the two-dimensional single crystalline structure of thin PZT films used in this study. Moreover, the use of polycrystalline PZT films to validate most models failed to fully capture the electrical characteristics of such films. This is due to the nonhomogenous structure, defects from grain boundaries, and misfit domains in such films. This model allows us to determine the equivalent acceptor doping density, N_a, due to Pb vacancies (V_{Pb}^{-2}). The model is based on similar models applied for metal−ferroelectric Schottky contacts that, however, do not take into account the voltage shift.[29−33]

The MFM structure used for the electrical characterization of the PZT films can be modeled as a superposition between surface charges from a remnant polarization and a back-to-back Shottky diode whereby two interface (top and bottom) capacitors are superpositioned on a bulk ferroelectric capacitor, as shown in Figure 3c,d. The PZT film is modeled as a wide bandgap p-type semiconductor with a ∼3.7 eV bandgap as determined from experiments and ab initio calculations.[24] The p-type characteristics of the film are due to the Pb vacancies, which act as acceptor impurities in the film. The defect reaction can be written as follows:

dx.doi.org/10.1021/nl302911k | Nano Lett. 2012, 12, 5455−5463

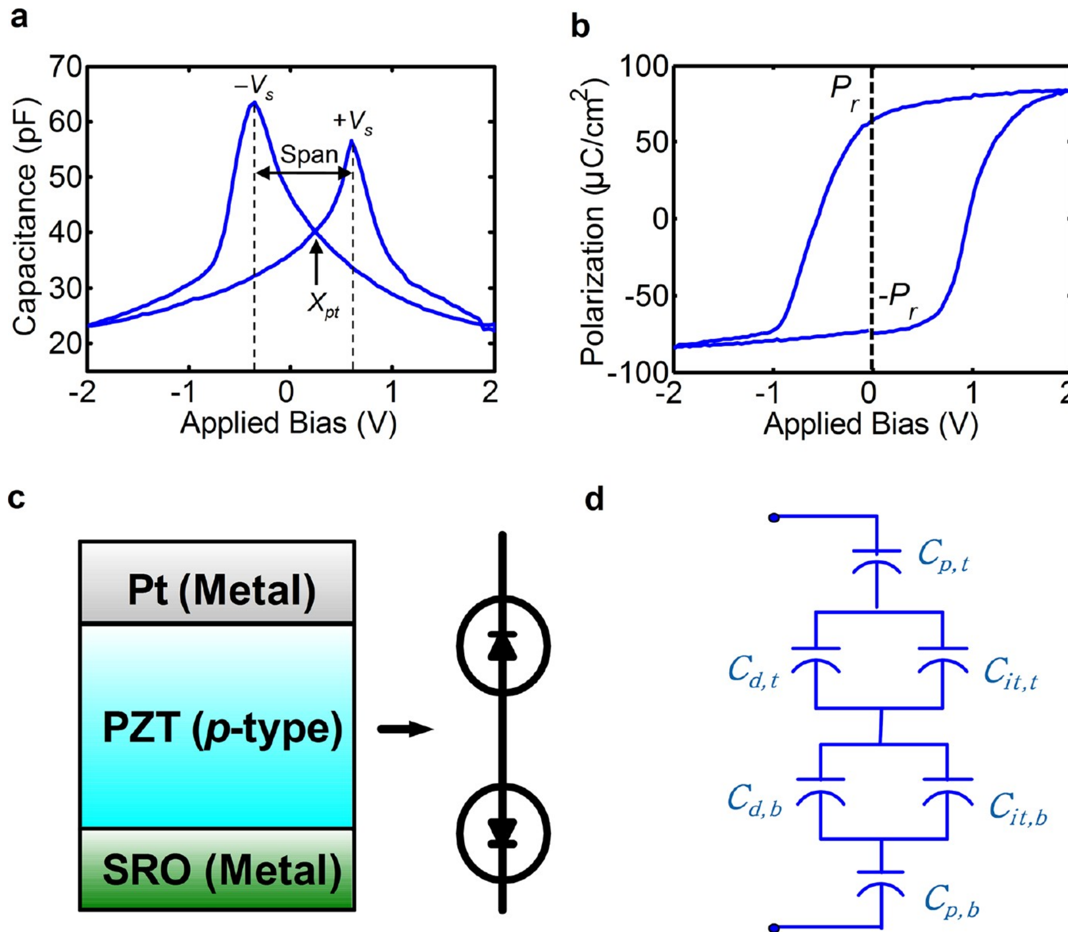

Figure 3. Electrical characterization of the 17 nm PZT film and back-to-back Schottky diode model. (a) Capacitance−voltage hysteresis loop. (b) Polarization−voltage hysteresis loop. (c) Schematic drawing of the metal−ferroelectric−metal (MFM) system. (d) MFM equivalent circuit including the depletion charge (C_d), polarization charge (C_p), and interface-trap charge (C_{it}) capacitances. The indices t and b refer to top and bottom electrodes.

$$\mathrm{Pb_{Pb}} \leftrightarrow \mathrm{Pb} + \mathrm{V_{Pb}^{-2}} + 2\mathrm{h}^{+} \tag{1}$$

where $\mathrm{Pb_{Pb}}$ denotes lead in the lattice whereas $\mathrm{V_{Pb}^{-2}}$ denotes the Pb vacancy in the PZT crystal. As mentioned previously, Pb has a high partial pressure and can readily evaporate from lattice sites leaving vacancies behind. These vacancies are the origin of the near surface concentration of negative trapped charges, which induce the remnant polarization that causes the built-in electric field.

In Schottky metal−semiconductor contacts, the depletion capacitance (C_d) from a small AC signal is defined as:[34]

$$C_d = \frac{\varepsilon_r \varepsilon_o A}{W} = \frac{\varepsilon_r \varepsilon_o A}{\sqrt{\frac{2\varepsilon_r \varepsilon_o}{qN_a}(V_{bi} - V_A)}} \tag{2}$$

where ε_r is the dielectric constant of the PZT film, ε_0 is the permittivity of the free space, A is the electrode area, N_a is the equivalent acceptor doping density, V_{bi} is built-in potential of the Schottky barrier, V_A is the applied bias, and q is the charge. The built-in potential for the Schottky barrier is defined as:[34]

$$V_{bi} = \frac{\chi_{PZT}}{q} + \left(\frac{E_{C(PZT)} - E_{F(PZT)}}{q}\right) - \frac{\phi_M}{q} \tag{3}$$

where χ_{PZT}, $E_{C(PZT)}$, and $E_{F(PZT)}$ are the affinity, conduction band, and Fermi energies of the p-type PZT film, whereas ϕ_M is the metal work function of the top/bottom electrode. As the bias is varied, the total capacitance of the back-to-back Schottky diode will be composed of reversed and forward biased junction capacitances corresponding to up and down polarizations, respectively. When the remnant polarization is saturated in one direction, the interface capacitance (C_p) of polarization charges within an ultrathin layer from the metal electrode, referred to as dead layer δ, will remain the same without polarization reversal:

$$C_p = \frac{\varepsilon_r \varepsilon_o A}{\delta} \tag{4}$$

The equivalent circuit for the back-to-back Schottky diode is shown in Figure 3d. The C_p and C_d of the forward biased junction are much larger than those of the reverse biased junction and can thus be ignored in series. An additional interfacial capacitance C_{it} originating from interface traps can coexist in parallel with C_d if reactive (oxidizing) metals such as Ti are used as electrodes.

The flat-band voltage shift due to these trap charges is given by Gauss's law:

$$\Delta V_f = -\frac{Q_f}{C_p} = -\frac{1}{C_p}\left[\frac{1}{\delta}\int_0^{\delta} x\rho(x)\mathrm{d}x\right] \tag{5}$$

where $\rho(x)$ is the charge density per unit volume, Q_f is the polarization in the interface regime between the metal and PZT

films, and C_p is the polarization capacitance. ΔV_f is sensitive to the exact position of the polarization. Ideally, polarization charges are located in the homogeneous interface regime near the metal contact region as assumed in this model. For instance, the negative remnant polarization charge ($-P_r$) is equivalent to an added negative applied bias to the semi-conducting PZT film and vice versa for $+P_r$. Therefore, an additional positive (negative) bias can achieve the same original band-bending. The difference in positive and negative switching biases (Figure 2a) can be fully described by ΔV_f in eq 5.

Furthermore, the total capacitance at reverse polarization gives rise to a discontinuity at the capacitance peaks around the $+V_s$ and $-V_s$ switching biases. In this regime, the thickness of the depletion layer in the bulk PZT film is almost the same as the dead layer thickness δ. Hence, δ can be extracted from this regime for both the top and the bottom contacts. The proposed model captures well the electrical characteristics of the ideal ferroelectric material where fast switching behavior is described by a fully rectangular polarization hysteresis loop with a constant remnant polarization charge and extremely sharp discontinuities in the C−V peaks indicating a zero dead layer thickness.

By applying this model to the C−V curve, the equivalent acceptor doping density N_a due to Pb vacancies (V_{Pb}^{-2}) can be determined. N_a is found to be $(1.62 \pm 0.26) \times 10^{15}$ cm^{-3} for $\chi_{PZT} = 3.5$ eV,[35] $\phi_{M(Pt)} = 5.3$ eV, and $\phi_{M(SRO)} = 5.2$ eV.[36] This is in very good agreement with Hall measurements performed on the same PZT film where a doping density of 1.47×10^{15} cm^{-3} was found. The reported variation in N_a represents the standard deviation of measurements across various electrodes.

The H_2 and O_2 plasma treatments, used to modify E_b, are performed in a plasma enhance chemical vapor deposition (PECVD) system (see Supporting Information). The plasma power and sample temperatures are kept constant at 500 W and 350 °C, respectively. On the other hand, gas type, gas flow, and pressure are varied. Table 1 summarizes the various treatment conditions.

Table 1. Gas Flow Rates and Pressures for Surface Treatments of PZT Films in the PECVD System

case	gas type	gas flow (sccm)	pressure (Torr)
I	He with 4% H_2	1000	0.5
II	He with 4% H_2	1000	1
III	O_2	100	0.5
IV	O_2	500	5

Figure 4a shows the $C-V$ hysteresis loop curves before (reference curve) and after the various H_2 plasma treatments, in which the pressure was varied while the flow rate was maintained at 1000 sccm (see Table 1). Under such oxygen poor conditions, the reduction reaction of Pb film can extract O atoms from the PZT top surface, and O vacancy formation is very stable.[24] The positive charges induced from the formation of O vacancies compensate for the already existing negative charges induced by the Pb vacancies. This, in turn, reduces (case I: 0.5 Torr pressure condition) and even suppresses (case II: 1 Torr pressure condition) the built-in electric field, making the $X_{pt} \cong 0$ V (initially $X_{pt} \cong 0.25$ V).

Note also that the positive switching bias $+V_s$ (0.6 V) remained unchanged after the H_2 plasma treatments irrespective of the treatment pressure. The negative switching bias $-V_s$, on the other hand, shifted negatively as the pressure was increased, which indicates that it is strongly proportional to the amount of O vacancies created as the pressure is increased. The O vacancies are thus compensating for the initial polarization to account for the observed negative shift in $-V_s$. In fact, at the 1 Torr pressure condition, that is, $X_{pt} \cong 0$ V, the magnitudes of $+V_s$ (0.6 V) and $-V_s$ (−0.5 V) switching biases are almost equal to one another, which strongly suggests the return to quasi-symmetry of the MFM system. The 0.1 V difference between $+V_s$ and $-V_s$ switching biases is very likely due to the 0.1 eV work-function difference between Pt and SRO electrodes. Therefore, this difference still induces an intrinsic asymmetry (although mild) that affects the switching behavior of the system and makes the behavior in up and down polarization cases mildly different even after Pb vacancy compensation. This is in agreement with ab initio studies on Pt-ferroelectric/dielectric-SRO[37,38] and SRO-ferroelectric-SRO systems[39,40] whereby such a small work-function difference can affect the system behavior.

The above observations indicate that the H_2 plasma treatment mainly reacted with the PZT surface. In other words, O vacancies were mainly formed at the PZT surface. Therefore, the positive charges induced by the O vacancies compensated for the negative charges induced by the Pb vacancies, which, as previously mentioned, would form only at the surface due to the high Pb partial pressure. This confirms that the built-in electric field problem is a surface chemistry problem that can be mitigated via a Pb redox process. Note that the H_2 plasma treatment can also trigger OH^- ions as previously seen in $LiTaO_3$ films.[41] However, such ions would positively shift the $C-V$ curves and increase the built-in electric field shift which is opposite to what we have observed. Therefore, OH^- ion formation is excluded from our study.

Figure 4b shows the $C-V$ hysteresis loop curves before (reference curve) and after the various O_2 plasma treatments, in which both pressure and gas rate where varied (see Table 1). As seen from the previous section, under such oxygen-rich conditions, the formation energies of O vacancies are highly positive and are thus unstable. The O_2 plasma treatments oxidize Pb in the PZT film, thereby filling the O vacancies that might have already existed in the film. This leads to an increase of negative charges induced by the Pb vacancies, which in turn shifts the $C-V$ curve and hence increases the built-in electric field (X_{pt} moved from 0.25 V to 0.30 V). Increasing the pressure and gas flow increases further the built-in electric field, thereby exacerbating its effect (case III to case IV). Unlike the H_2 plasma treatments, however, both $+V_s$ (0.8 V) and $-V_s$ (−0.2 V) switching biases have shifted positively, which is indicative that the oxidation process taking place was throughout the PZT film and not just at the surface as concluded for the H_2 plasma treatments.

To confirm that the redox/vacancy activity is at the origin of the built-in electric field change, we also performed a XPS characterization of the same PZT film after O_2 and H_2 plasma treatments. The XPS technique is surface-sensitive with a probing depth in the range of 2−5 nm and therefore can only provide information at the near surface of the PZT film. This, however, should provide ample information as the redox/vacancy activity is mainly at the PZT surface as concluded by the electrical $C-V$ characterization. Figure 4c,d shows XPS spectra after H_2 and O_2 plasma treatments, respectively. From these curves, the percentage of reduced Pb is 3.5% of the total Pb after the H_2 plasma treatment. On the other hand, the reduced Pb percentage after the O_2 plasma treatment decreased

dx.doi.org/10.1021/nl302911k | Nano Lett. 2012, 12, 5455−5463

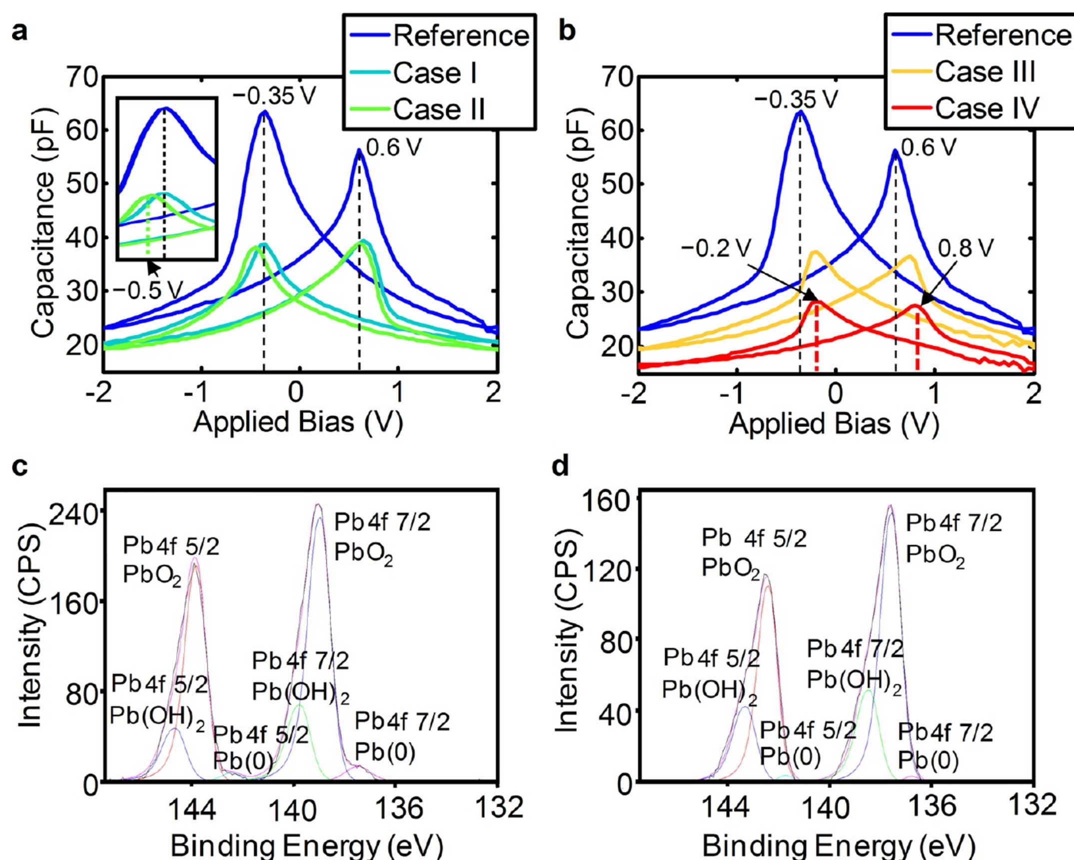

Figure 4. Effect of H_2 (a) and O_2 (b) plasma treatments on $C-V$ hysteresis loop curve. (a) E_b decreased after each treatment up to full suppression (X_{pt} shifted from 0.25 to 0 V), which is indicative of Pb reduction or O vacancy formation. The inset shows a zoom-in of the C−V curve to better visualize the shift in $-V_s$ from −0.35 V to −0.5 V after H_2 plasma treatment (case II). $+V_s$ did not shift during the treatment. (b) E_b increased after each treatment (X_{pt} shifted from 0.25 to 0.30 V), which is indicative of Pb oxidation or O vacancy filling. Both $+V_s$ (from 0.6 to 0.8 V) and $-V_s$ (from −0.35 to −0.2 V) shifted to the right after O_2 plasma treatments. Treatment conditions for each case are given in Table 1. (c) XPS spectra of PZT films after H_2 plasma treatment. (d) XPS spectra of PZT films after O_2 plasma treatment (case IV). After the H_2 plasma treatment, the percentage of reduced Pb was 3.5% of the total Pb. It then reduced to 1.3% of the total Pb after the O_2 plasma treatment.

down to 1.3% of the total Pb. Moreover, the O/(Pb+Ti+Zr) ratio after the O_2 plasma treatment is measured to be 2.4%, whereas after the H_2 plasma it reduced down to 1.8%. Note that, despite all of the above observations, we cannot categorically refute the creation of O vacancies in the bulk during the H_2 plasma reduction treatment, especially given the thin (17 nm) PZT films used here. We, however, believe it to be minimal.

The $C-V$ model is also used to extract the equivalent doping density of the PZT film for case I (1000 sccm of He with 4% H_2 at 0.5 Torr) and case III (100 sccm of O_2 at 0.5 Torr) (see Table 1 for details). For case I, the *p*-type doing density reduced from 1.62×10^{15} cm^{-3} to 7.45×10^{14} cm^{-3}. This is strongly indicative that charge compensation via O vacancies has occurred, thereby diluting the acceptor carriers and reducing the *p*-type doing density. For case II, on the other hand, the acceptor doping density increased from 1.62×10^{15} cm^{-3} to 3.14×10^{15}. This increase confirms that the oxygen-rich environment provided by the O_2 plasma treatment fills any existing O vacancy that might have compensated for the positive charges from the already existing Pb vacancies. The change in doping densities associated with the H_2 and O_2 plasma treatments is also indicative of changes in film conductivity.

The preceding facts strongly support the conclusion that the redox/vacancy activity at the surface is at the origin of the built-in electric field change. Shifts in C−V curves after H_2 and O_2 plasma treatments demonstrate the fact that Pb and O vacancies can be regarded as trapped charges that compensate for the total polarization of PZT films. These treatments can be used to modulate and suppress the built-in electric, thereby enabling the writing of stable and equal size sub-10 nm domains in upward and downward polarized PZT ferroelectric films (see next section). Moreover, the negative switching bias $-V_s$ on the top Schottky contact is shown to be a strong function of the Pb redox process, which can also be modulated via these plasma treatments to restore quasi-symmetry to the MFM system.

Finally, we would like to point out that we performed electrical characterization on the MFM systems after ∼24 h of each plasma treatment without seeing any noticeable effects from the initial $C-V$ curves, which were also taken ∼16 h after the treatments. In addition, the XPS analysis was performed a few days after the treatments, which clearly captures the Pb redox and compensation processes. This confirms that the redox process induced by these treatments is not transient and can provide long-term stability that is needed in actual probe-based memory technologies. This is also in agreement with ab initio studies where the formation of Pb and O vacancies is

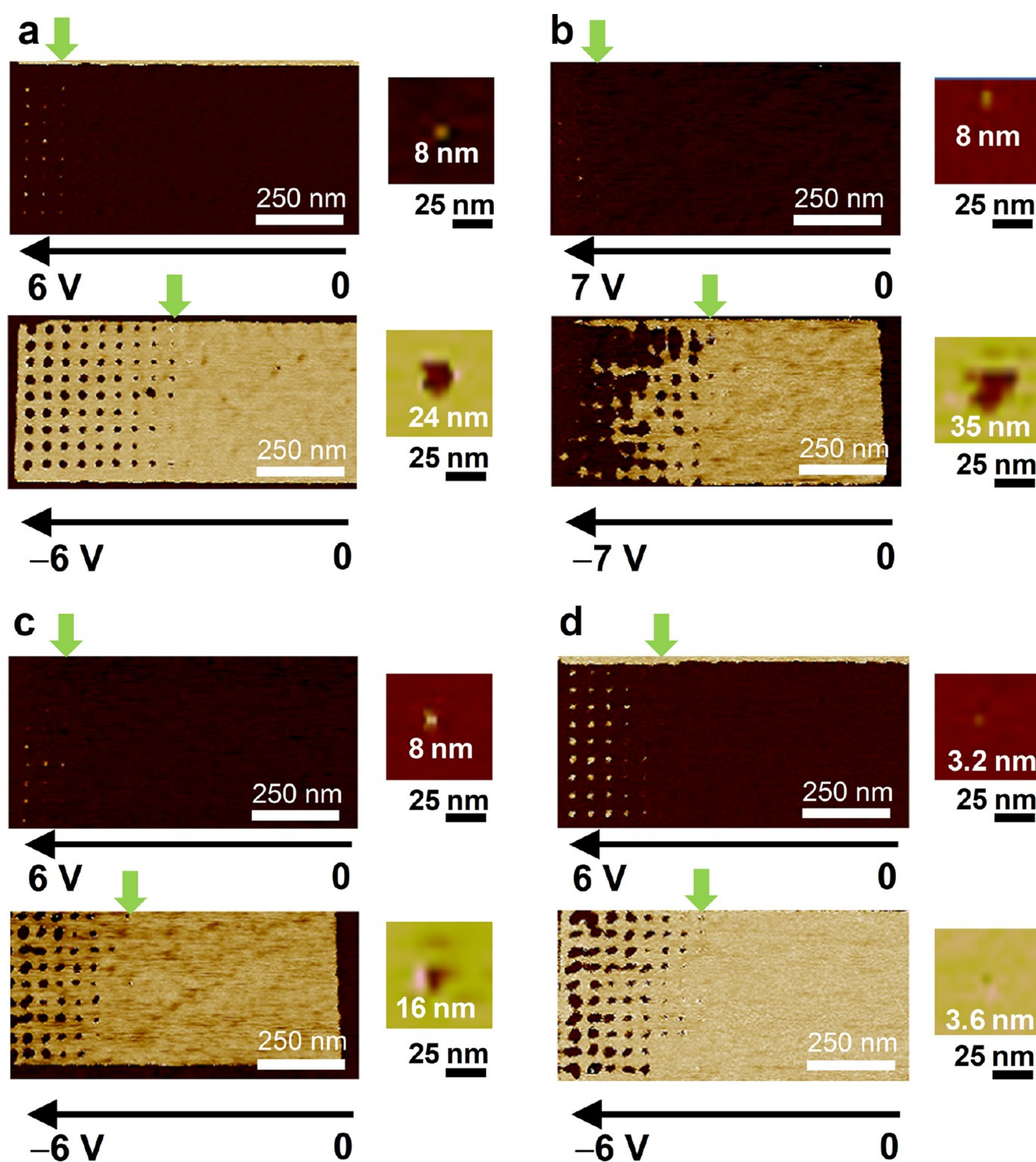

Figure 5. Effects of H_2 and O_2 plasma treatments on bit writing. PFM phase images of inverted domains written on up (top image) and down (bottom image) polarized sections of the same PZT film in its (a) as-received conditions, (b) after 3 min of O_2 plasma, (c) after 2 min of H_2 plasma, and (d) after 4 min of H_2 plasma. The pulse bias was increased by small increments along the width of the sections to determine the threshold (smallest) voltage at which stable bits are written. The green arrows highlight the threshold voltage writing location. The insets to the right of each section are zoom-in views of the smallest stable bits written at these threshold voltages. See text for details.

predicted to affect the polarization properties without any significant effect on the fatigue properties of PZT crystals.[42,43] This phenomenon was also observed experimentally.[44,45]

The E_b tuning mechanism is also used to enable the writing of stable and equal size sub-10 nm domains in up and down polarized PZT films. This is very important for ultrahigh density probe-based memory devices using ferroelectric media. The films are 17 nm thick with an atomically smooth surface (0.20 nm RMS roughness), possess an initial built-in electric field of 2.3×10^7 V/m, and are initially up-polarized. Figure 5a shows piezoresponse force microscopy (PFM) phase images of inverted domains written on up (top image) and down (bottom image) polarized sections of the same PZT film in its as-received conditions, that is, prior to any treatment. The initially down-polarized section of the film was obtained by poling the film at a very high positive bias applied continuously to the probe-tip as it was scanning the surface of the section. A matrix of inverted domains was then written (see Supporting Information for procedure) on both sections of the sample by applying bias pulses varying from 0 to 6 V for the up-polarized section and from 0 to −6 V for the down-polarized section. The pulse bias was increased by small increments along the width of the sections as depicted in Figure 5a. In what follows, the threshold voltage is defined as the smallest applied pulse bias at which a stable bit is written which will not invert back to its initial polarization.[12] The definition of threshold voltage used here is only from a "technology-enabling point of view" and might differ from definitions used by other researchers.

For the up-polarized section where the built-in electric field is antiparallel to bit writing, the threshold voltage was 5 V. Under this bias condition, the bit is 8 nm in size. For the down-polarized section, on the other hand, the threshold voltage was

dx.doi.org/10.1021/nl302911k | Nano Lett. 2012, 12, 5455−5463

only −3.5 V with a bit size of 24 nm. In this case, the built-in electric field is in the same direction as the applied electric field and is therefore added to it, enabling very large bits to be written at relatively low biases.

The 8 nm bit obtained in the up-polarized section under the 5 V threshold voltage is predicted to be energetically stable under the effects of ferroelectric depolarization field (responsible for the critical thickness mentioned previously), domain wall energy, and built-in electric field. The prediction is obtained by a procedure we previously developed,[12] which combines electrostatic simulation and energetic analysis. The procedure consists of estimating the speed of inverted domain evolution which is proportional to the energy driving force, that is, the total free energy reduction rate with respect to the change in domain size. The change in energy associated with the introduction of a 180° inverted domain or inclusion, Ω, in a ferroelectric material is given by:[12,46]

$$\Delta T = -\frac{1}{2}\iiint_{\Omega} E_i P_i^* \mathrm{d}v - \iiint_{\Omega} E_i^0 P_i^* \mathrm{d}v + \Gamma(x, y, z)\gamma \quad (6)$$

where E_i^0 is the electric field applied in the absence of inclusion, and E_i is due to the spontaneous polarization prescribed in the inclusion. P_i^* is the spontaneous polarization within the inclusion, which is equal to $-2\vec{P}_S$, where $\vec{P}_S$ is the spontaneous polarization within the uniformly polarized ferroelectric material. Γ is the surface area of the inverted domain, and γ is the surface energy per unit area of the domain wall. The size and shape of the inverted domain, Ω, are determined by the modeling of the electric field component along the polarization axis using the COMSOL-MULTTIPHYSICS package. The probe-tip is modeled as a metallic wire in contact with the PZT film on a grounded metallic electrode. The properties of the PZT films determined experimentally are used in the simulations. The experimental bias is applied to the electrode and fixed charge, and fixed field assumptions are adopted. Axial symmetry is also assumed in the model. For the inverted domain to remain stable, the free energy reduction rate associated with the spherical domain, $f = -(\partial \Delta T/\partial a)$, has to be positive. More information about the stability prediction analysis can be found in ref 12.

The sample was then treated using O_2 plasma for 3 min generated at 50 W of power and under a 0.5 Torr pressure. Under these O_2 plasma conditions, the built-in electric field is increased as discussed in previous sections. After such a treatment, the same writing procedure was repeated on up- and down-polarized sections of the PZT sample (Figure 5b). Only this time the bias pulse was varied from 0 to 7 V to accommodate for the high (6 V) threshold voltage that enabled stable bit writing on the up-polarized section. Although, the size of the bit was 8 nm, it was written at a higher bias. This is as expected due to the larger E_b present in the film. For the down-polarized section, the threshold voltage remained the same at −3.5 V. However, the smallest written bit increased to 35 nm, with bits merging with each other for higher pulse biases, which is indicative of the large E_b increase.

The sample was further treated using H_2 plasma for 2 min generated at 50 W of power and under a 0.5 Torr pressure. Under these H_2 plasma conditions, E_b decreases as discussed in previous sections. The same writing procedure as with the as-received sample was repeated on up- and down-polarized sections of the PZT sample (Figure 5c). The threshold voltage that enabled stable bit writing on the up-polarized section returned down to the initial 5 V value, which is indicative of a lesser E_b effect. At this bias, the size of the stable bit was again 8 nm. For the down-polarized section, on the other hand, the threshold voltage increased to −4.5 V. This is also indicative of a decrease in E_b as a larger applied electric field was applied to compensate for this decrease. The bit size written at the threshold voltage decreased compared to the previous two cases and was only 16 nm.

Ideally, both up- and down-polarized sections should possess the same magnitude of threshold voltage, enabling the writing of equal size bits in the two sections. This case can only be achieved when E_b is suppressed. To reach this state, we performed an additional 2 min of H_2 plasma treatment under the same power and pressure conditions. The same writing procedure was repeated again (Figure 5d). The threshold voltage on the up-polarized section was further reduced down to 4.9 V for which bits as small as 3.2 nm were written, that is, 8 unit-cell size. Such a domain size corresponds to potential 60 $\mathrm{Tbit/in^2}$ storage densities, which, to the best of our knowledge, is the smallest stable inverted volume ever written on ferroelectric films. For the down-polarized section, the threshold voltage increased to −4.6 V, which is about the same voltage on the up-polarized section. The bit size at this bias also reduced down to 3.6 nm, which is also about the same size on the up-polarized section. This is strongly indicative that the zero E_b state was achieved.

We have also investigated creep effects related to the sub-10 nm inverted domains achieved in this study by rereading the domains after 24 h. Creep is due to competition between the elastic energy of the propagating interface and a pinning potential that might affect domain size or stability.[47] However, we have not observed any significant size change, which is in very good agreement with previous studies[47,48] where creep was only observed for inverted domains written under bias pulse widths larger than 20 μs; that is, the creep effect depends on the pulse duration. In the current study, the write operations were performed at a bias pulse width of only 500 ns. Therefore, the switching time associated with the propagating interface of the nanodomain is directly related to the pulse width, which has to be optimized to prevent nanodomain creep. Moreover, the radius of all probe-tips used in this study was also maintained at 20 ± 3 nm. These small probe-tips enable the confinement of the electric field to a very small area, which would limit the creep effect as also noted in ref 47. In addition, previous studies have shown that, under large and concentrated electric fields, such as those applied in the writing of the sub-10 nm inverted domains, O vacancies in perovskites films become highly mobile through the film thickness.[49] Therefore the O vacancies created by the H_2 plasma treatments are very likely to redistribute through the film thickness during the writing process. This redistribution phenomenon improves the stability of the inverted domains. This is because an O vacancy can lower its energy when it coincides with the inverted domain wall without causing film fatigue,[42,43] acting as a pinning site for the wall as predicted by ab initio studies,[50] thereby providing increased stability to inverted domains.[51]

In summary, we have demonstrated that the built-in electric field in high quality, atomically smooth, single crystalline PZT films is due to near-surface trapped negative charges. We have used O_2 and H_2 plasma treatments to oxidize/reduce the PZT surface, thereby altering the electrochemistry of the Pb overlayer. These treatments compensate for the negative charges induced by the Pb vacancies and thus reduce the

built-in electric field. By varying the plasma conditions, the PZT surface was oxidized or reduced in small increments to allow fine-tuning and suppression of the built-in electric field. This tuning mechanism was verified by electrical and XPS characterizations of the treated PZT films. Finally, this tuning mechanism was used to demonstrate the writing of stable and equal size sub-4 nm domains in up and down-polarized PZT films, which is an important milestone toward the development of ultrahigh density probe-based memory devices using ferroelectric media. Such portable and low power storage devices will be ideal for emergent technologies, such as DNA sequencing systems,[52] which generate a large amount of data and that ultimately can become portable.

■ ASSOCIATED CONTENT

Ⓢ Supporting Information

PZT ferroelectric film growth, electrical characterization of PZT film, plasma treatments, and data write and read. This material is available free of charge via the Internet at http://pubs.acs.org.

■ AUTHOR INFORMATION

Corresponding Author

*E-mail: noureddine.tayebi@intel.com.

Notes

The authors declare no competing financial interest.

■ REFERENCES

(1) Ramesh, R.; Aggarwal, S.; Auciello, O. *Mater. Sci. Eng.* **2001**, *32*, 191.
(2) Ishiwara, H.; Okuyama, M.; Arimoto, Y. *Ferroelectric Random Access Memories: Fundamentals and Applications*; Springer: New York, NY, 2004.
(3) Ahn, C. H.; Tybell, T.; Antognazza, L.; Char, K.; Hammond, R. H.; Beasley, M. R.; Fischer, O.; Triscone, J.-M. *Science* **1997**, *276*, 1100.
(4) Ahn, C. H.; Rabe, M. R.; Triscone, J.-M. *Science* **2004**, *303*, 488.
(5) Cho, Y.; Hashimoto, S.; Odagawa, N.; Tanaka, K.; Hiranaga, Y. *Nanotechnology* **2006**, *17*, S137.
(6) Cho, Y.; Hashimoto, S.; Odagawa, N.; Tanaka, K.; Hiranaga, Y. *Appl. Phys. Lett.* **2005**, *87*, 232907.
(7) Cho, Y.; Fujimoto, K.; Hiranaga, Y.; Wagatsuma, Y.; Onoe, A.; Terabe, K.; Kitamura, K. *Nanotechnology* **2003**, *14*, 637.
(8) Garcia, V.; Fusil, S.; Bouzehouane, K.; Enouz-Vedrenne, S.; Mathur, N. D.; Barthélémy, A.; Bibes, M. *Nature* **2009**, *460*, 81.
(9) Tayebi, N.; Yoshie, N.; Chen, R. C.; Collier, P. C.; Giapis, K. P.; Zhang, Y. *Appl. Phys. Lett.* **2008**, *93*, 103112.
(10) Forrester, M. G.; Ahner, J. W.; Bedillion, M. D.; Bedoya, C.; Bolten, D. G.; Chang, K.-C.; de Gersem, G.; Hu, S.; Johns, E. C.; Nassirou, M.; Palmer, J.; Roelofs, A.; Siegert, M.; Tamaru, S.; Vaithyanathan, V.; Zavaliche, F.; Zhao, T.; Zhao, Y. *Nanotechnology* **2009**, *20*, 225501.
(11) Heck, J.; Adams, D.; Belov, N.; Chou, T. A.; Kim, B.; Kornelsen, K.; Ma, Q.; Rao, V.; Severi, S.; Spicer, D.; Tchelepi, G.; Witvrouw, A. *Microelectron. Eng.* **2010**, *87*, 1198.
(12) Tayebi, N.; Narui, Y.; Franklin, N.; Collier, C. P.; Giapis, K. P.; Nishi, N.; Zhang, Y. *Appl. Phys. Lett.* **2010**, *96*, 023103.
(13) Junquera, J.; Ghosez, P. *Nature* **2003**, *422*, 506−509.
(14) Despont, L.; Koitzsch, C.; Clerc, F.; Garnier, M. G.; Aebi, P.; Lichtensteiger, C.; Triscone, J.-M.; Garcia de Abajo, F. J.; Bousquet, E.; Ghosez, P. *Phys. Rev. B* **2006**, *73*, 094110.
(15) Fong, D. D.; Stephenson, G. B.; Streiffer, S. K.; Eastman, J. A.; Auciello, O.; Fuoss, P. H.; Thompson, C. *Science* **2004**, *304*, 1650−1653.
(16) Lichtensteiger, C.; Dawber, M.; Stucki, N.; Triscone, J.-M.; Hoffman, J.; Yau, J.-B.; Ahn, C. H.; Despont, L.; Aebi., P. *Appl. Phys. Lett.* **2007**, *90*, 052907.
(17) Kim, Y. S .; Kim, D. H.; Kim, J. D.; Chang, Y. J.; Noh, T. W.; Kong, J. H.; Char, K.; Park, Y. D.; Bu, S. D.; Yoon, J.-G.; Chung, J.-S. *Appl. Phys. Lett.* **2005**, *86*, 10290.
(18) Petraru, A.; Kohlstedt, H.; Poppe, U.; Waser, R.; Solbach, A.; Klemradt, U.; Schubert, J.; Zander, W.; Pertsev, N. A. *Appl. Phys. Lett.* **2008**, *93*, 072902.
(19) Hau, S. K.; Wong, K. H. *Appl. Phys. Lett.* **1995**, *66*, 245.
(20) Li, X.; Mamchik, A.; Chen, I.-W. *Appl. Phys. Lett.* **2001**, *79*, 809.
(21) Wang, B.; Woo, C. H. *J. Appl. Phys.* **2003**, *94*, 610.
(22) Miura, K.; Tanaka, M. *Jpn. J. Appl. Phys.* **1996**, *35*, 2719.
(23) Eichel, R. A. *J.Electroceram.* **2007**, *19*, 9.
(24) Zhang, Z.; Wu, P.; Lu, L.; Shu, C. *Appl. Phys. Lett.* **2006**, *88*, 142902.
(25) Zhang, Z.; Wu, P.; Lu, L.; Shu, C. *J. Alloys Compd.* **2008**, *449*, 362.
(26) Zhukovskii, Y. F.; Kotominb, E. A.; Piskunov, S.; Ellis, D. E. *Solid State Commun.* **2009**, *149*, 1359.
(27) Chen, Y.; McIntyre, P. C. *Appl. Phys. Lett.* **2007**, *91*, 072910.
(28) Chen, Y.; McIntyre, P. C. *Appl. Phys. Lett.* **2007**, *91*, 232906.
(29) Pintiliea, L.; Alexe, M. *J. Appl. Phys.* **2005**, *98*, 124103.
(30) Pintiliea, L.; Boerasu, I.; Gomes, M. J.; Zhao, T.; Ramesh, R.; Alexe, M. *J. Appl. Phys.* **2005**, *98*, 124104.
(31) Sze, S. M. *Physics of Semiconductor Devices*, 2nd ed.; John Wiley & Sons: New York, NY, 1981; Chapters 7 and 10.
(32) Goren, D.; Amir, N.; Nemirovsky, Y. *J. Appl. Phys.* **1992**, *71*, 318.
(33) Goren, D.; Nemirovsky, Y. *J. Appl. Phys.* **1995**, *77*, 244.
(34) Muller, R. S.; Kamins, T. I. *Device Electronics for Integrated Circuits*, 3rd ed.; John Wiley & Sons: Hoboken, NJ, 2007.
(35) Scott, J. F.; Watanabe, K.; Hartmann, A. J.; Lamb, R. N. *Ferroelectrics* **1999**, *225*, 83.
(36) Fang, X.; Kobayashi, T. *Appl. Phys. A* **1999**, *69*, S587.
(37) Stengel, M.; Spaldin, N. A. *Phys. Rev. B* **2007**, *75*, 205121.
(38) Liu, X.; Wang, Y.; Lukashev, P. V.; Burton, J. D.; Tsymbal, E. Y. *Phys. Rev. B* **2012**, *85*, 125407.
(39) Zubko, P.; Stucki, N.; Lichtensteiger, C.; Triscone, J.-M. *Phys. Rev. Lett.* **2010**, *104*, 187601.
(40) Jo, J. Y.; Chen, P.; Sichel, R. J.; Callori, S. J.; Sinsheimer, J.; Dufresne, E. M.; Dawber, M.; Evans, P. G. *Phys. Rev. Lett.* **2011**, *107*, 055501.
(41) Gopalana, V.; Gupta, M. C. *J. Appl. Phys.* **1996**, *80*, 6099.
(42) Pöykkö, S.; Chadi, D. J. *Phys. Rev. Lett.* **1999**, *83*, 12.
(43) Pöykkö, S.; Chadi, D. J. *J. Appl. Phys. Lett.* **2000**, *76*, 499.
(44) Doi, H.; Atsuki, T. *Jpn. J. Appl. Phys., Part 1* **1995**, *34*, 5105.
(45) Du, X.; Chen, I.-W. *J. Appl. Phys.* **1998**, *83*, 7789.
(46) Wang, B.; Woo, C. H. *J. Appl. Phys.* **2003**, *94*, 610.
(47) Tybell, T.; Paruch, P.; Giamarchi, T.; Triscone, J.-M. *Phys. Rev. Lett.* **2002**, *89*, 097601.
(48) Paruch, P.; Giamarchi, T.; Triscone, J.-M. *Phys. Rev. Lett.* **2005**, *94*, 197601.
(49) Szot, K.; Speier, W.; Bihlmayer, G; Waser, R. *Nat. Mater.* **2006**, *5*, 312.
(50) He, L.; Vanderbilt, D. *Phys. Rev. B* **2003**, *68*, 134103.
(51) Paruch, P.; Kolton, A. B.; Hong, X.; Ahn, C. H.; Giamarchi, T. *Phys. Rev. B* **2012**, *85*, 214115.
(52) Rothberg, J. M.; Hinz, W.; Rearick, T. M.; Schultz, J.; Mileski, W.; Davey, M.; Leamon, J. H.; Johnson, K.; Milgrew, M. J.; Edwards, M.; Hoon, J.; Simons, J. F.; Marran, D.; Myers, J. W.; Davidson, J. F.; Branting, A.; Nobile, J. R.; Puc, B. P.; Light, D.; Clark, T. A.; Huber, M.; Branciforte, J. T.; Stoner, I. B.; Cawley, S. E.; Lyons, M.; Fu, Y.; Homer, N.; Sedova, M.; Miao, X.; Reed, B.; Sabina, J.; Feierstein, E.; Schorn, M.; Alanjary, M.; Dimalanta, E.; Dressman, D.; Kasinskas, R.; Sokolsky, T.; Fidanza, J. A.; Namsaraev, E.; McKernan, K. J.; Williams, A.; Roth, G. T.; Bustillo, J. *Nature* **2011**, *475*, 348.